ACS OMEGA

Article

Cite This: ACS Omega 2019, 4, 4243−4251

http://pubs.acs.org/journal/acsodf

Facet-Dependent Photodegradation of Methylene Blue Using Pristine CeO_2 Nanostructures

Deblina Majumder,[†] Indranil Chakraborty,[‡] Kalyan Mandal,[‡] and Somenath Roy*[,†]

[†]CSIR-Central Glass and Ceramic Research Institute, 196, Raja S.C. Mullick Road, Kolkata 700032, West Bengal, India

[‡]S. N. Bose National Centre for Basic Sciences, Block JD, Sector III, Salt Lake, Kolkata 700106, India

Supporting Information

ABSTRACT: This work comprises the shape- and facet-dependent catalytic efficacies of different morphologies of CeO_2, namely, hexagonal, rectangular, and square. The formation of different shapes of CeO_2 is controlled using polyvinyl pyrrolidone as a surfactant. The surface reactivity of formation of differently exposed CeO_2 facets is thoroughly investigated using UV−visible, photoluminescence, Raman, and X-ray photoelectron spectroscopies. A correlation between the growth of a surface-reactive facet and the corresponding oxygen vacancies is also established. Considering the tremendous contamination, caused by the textile effluents, the present study articulates the facet-dependent photocatalytic activities of pristine CeO_2 for complete degradation of methylene blue within 175 min. The observed degradation time deploying pristine CeO_2 as a catalyst is the shortest to be reported in the literature to our best knowledge.

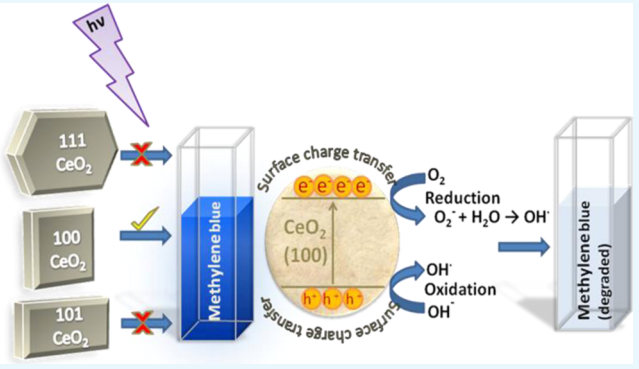

INTRODUCTION

Synthetic dyes are found in a wide range of products such as clothes, leather accessories, and furniture. However, a side effect of their widespread use is that up to 12% of these dyes are wasted during the dying process and about 20% of this wastage enters the environment (mainly into water supply). Water contamination from the textile industries is one of the major threats in the present time as a side effect of the widespread use of dyes which are hugely wasted and reportedly 20% of that wastage comes to the environment directly via water.[1] It is a terrifying fact that during the dying process, about 15% of the total world production of dyes are released as textile effluents which irreparably damage the eco system and which is a dangerous source of nonaesthetic pollution, eutrophication, and agitation in aquatic life.[2] Especially for the third-world countries, the purification of dye-contaminated water is one of the most challenging environmental problems. The existing conventional treatments like chemical coagulation or adsorption do not serve the purpose satisfactorily as they convert the dyes from the liquid to the solid phase which requires further treatment and the effective cost of the process increases as well.[3] In the last few years, photocatalysis has come up to be a promising and widely accepted method for the treatment of waste water-containing dyes.[4,5] The dyes that come from the textile wastage are majorly azo-dyes in nature and prone to photocatalytic degradation under UV irradiation where the semiconductor metal oxides or sulphides provide oxidizing radicals causing the degradation. Among all the available materials, cerium oxide semiconductor metal oxides are of high choice because of their highest abundance in nature and tunable oxidizing property, resulting from facile transition between Ce^{4+} and Ce^{3+}.[6,7] The surface redox efficacies of ceria are greatly dependent on their surface defects which are highly influenced by their crystallographic structures and morphologies. Different shapes expose different active planes of ceria, differing in their performance in surface catalysis. (100), (110), and (111) are the three low-index lattice planes of ceria, and according to density functional theory (DFT) calculations, their reactivity order follows the order (100) > (110) > (111).[8−11] It implies that the generation of oxygen vacancies, favorable for catalytic activity, is higher in the structures where the (100) plane is exposed than that in (110) and (111).[12] The exposure of different planes depends on the shapes of nanoparticles. Reportedly, formation of octahedral or truncated octahedral shapes is associated with most stable exposed (111) facets,[13] whereas the nanocube-like structures correspond to the most surface active (100) plane.[14] In the last few years, there are numerous reports on the photocatalytic degradation of textile dyes using doped, undoped, or composites of ceria.[15] Pouretedal et al. described the process of methylene blue (MB) degradation using bare CeO_2 at different pH values, though complete degradation was not obtained in their case.[16] Upto 70% degradation of MB is investigated using three-dimensional ordered macroporous CeO_2 prepared on the

Received: November 27, 2018
Accepted: February 12, 2019
Published: February 26, 2019

DOI: 10.1021/acsomega.8b03298
ACS Omega 2019, 4, 4243−4251

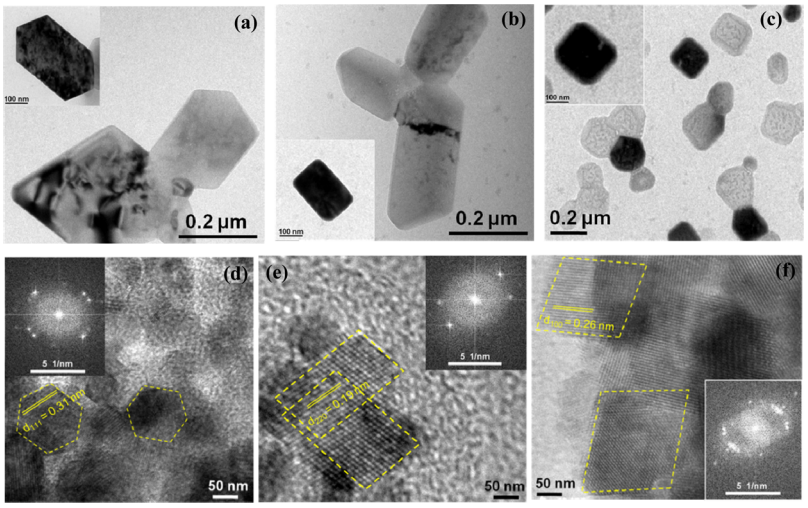

Figure 1. Morphological analysis, (a–c) TEM micrographs of hexagonal, rectangular, and cuboidal ceria with {111}, {110}, and {100} exposed facets, namely, Ce-1, Ce-2, and Ce-3, respectively, (d–f) HRTEM images, showing the lattice fringes of (111), (110), and (100) plane (inset FFT) of the mentioned Ce-1, Ce-2, and Ce-3, respectively.

fluorine-doped tin oxide substrates.[17] Channei and his group reported the catalytic efficiency of Fe-doped ceria quenching of the band gap after doping.[18] The complete degradation time of MB is reduced from 23 to 14 h using samarium- and gadolinium-doped CeO_2 nanoparticles instead of bare ceria.[19] Besides the doped CeO_2 materials, many mixed oxides, nanohybrids, and composites of cerium are widely ventured for the dye degradation purpose.[20−22] The present article delineates the shape-controlled synthesis process of ceria nanostructures with three different exposed low-index facets, resulting in hexagonal, rectangular, and cuboidal shapes. The formation mechanism is detailed, explaining the plausible role of polyvinylpyrrolidone (PVP) as a structure-directing additive. The semiconducting features of the crystallographic structures are well corroborated with their respective shapes and analyzed in the light of their photoluminescence (PL) property. The effect and influence of different morphologies, dominated by different crystallographic planes, are thoroughly investigated for their photocatalytic degradation efficiency of MB.

RESULTS AND DISCUSSION

Crystallographic and Morphological Analysis. The X-ray diffraction (XRD) patterns of synthesized materials Ce-1, Ce-2, and Ce-3 indicated the formation of a fluorite cubic structure (FCC) phase (JCPDS card no. 34-1394), provided in Figure S1. The crystallite size and lattice parameters of the samples were calculated using Scherrer eq 1

$$D = K\lambda/(\beta \cos \theta) \quad (1)$$

where K is a constant equal to 0.89, λ is the X-ray wavelength equal to 0.154 nm, β is the full width at half maximum, and θ is the half diffraction angle. Transmission electron microscopy (TEM) images reveal the morphology of the prepared CeO_2 materials. Figure 1a–c shows the formation of hexagonal, rectangular, and cuboidal type structures in Ce-1, Ce-2, and Ce-3, respectively. The corresponding high-resolution TEM (HRTEM) micrographs [with inset showing fast Fourier transform (FFT)] of Ce-1, Ce-2, and Ce-3 are presented in Figure 1d–f, respectively. The occurrence of different morphologies plays a pivotal role regarding the catalytic efficiency of the material. Again, the evolution of a morphology or shape of a material highly depends on the growth and orientation of crystallographic planes. Among the three low-index lattice planes of CeO_2, according to DFT calculations, the stability order follows the sequence (111) > (110) > (100), while the activity follows the reverse. In correlation with surface activities, the formation oxygen vacancies are also of paramount importance and the associated energy is different for differently exposed planes of CeO_2.[8−11] As shown in Figure 1, the different shapes of CeO_2 expose different lattice planes. In the case of Ce-1, a hexagonal structure, the (111) plane is exposed; for the rectangular Ce-2, the (110) plane is exposed; and for cuboidal Ce-3, the most surface-active (100) plane is found to be exposed. To minimize surface energy of the material, the formation of most stable exposed facet, (111) is highly favored. The individual TEM images of different shapes of different samples are also included in Figure S2. Performing the nitrogen adsorption–desorption isotherm study and determining Brunauer–Emmett–Teller (BET) surface area of the CeO_2 materials of different shapes, the Ce-3 nanostructures are found to possess the highest surface area of 897 cm^2/g among all (Figure 2). The respective isotherms of Ce-1 and Ce-2 are provided in the Supporting Information (Figure S3), and the details are summarized in Table 1. The

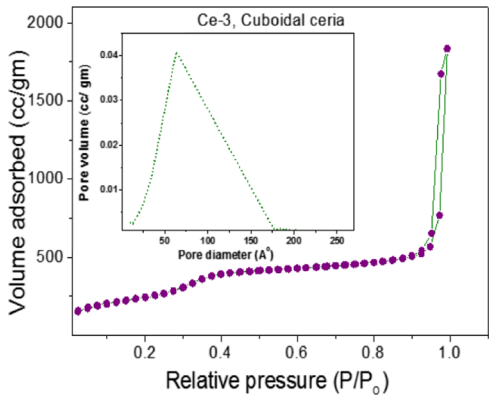

Figure 2. Nitrogen adsorption–desorption isotherm of Ce-3 with inset pore size distribution.

DOI: 10.1021/acsomega.8b03298
ACS Omega 2019, 4, 4243−4251

Table 1. Average Surface Area, Pore Volume, and Pore Diameter of Different Shapes of CeO_2 Nanostructures

samples	average surface area (cm^2/g)	average pore volume (cc/g)	average pore diameter (Å)
Ce-1, hexagonal CeO_2	235.4	2.534	∼9
Ce-2, rectangular CeO_2	265.8	2.846	∼5
Ce-3, cuboidal CeO_2	897.1	3.427	∼75

addition of more amount of PVP during synthesis of Ce-3 than that of in Ce-1 (5.04 times) and Ce-2 (2.52 times) may have played a vital role in making cuboidal CeO_2 a porous one upon evaporation and providing higher surface area than the rest two. CeO_2 has a fluorite structure and three commonly observed CeO_2 facets, (100), (110), and (111). The coordination states of the surface cation (Ce^{4+}) and anion (O^{2-}) differ on each surface. Generally, in CeO_2, the coordination numbers of Ce and O are 8 and 4, respectively. However, depending on the formation or predominant exposure of different facets, surface defects are developed. Reportedly,[22] for Ce^{4+}, the coordination numbers are 7, 6, and 6 for (111), (100), and (110), respectively, and for anions, they are 3, 2, and 3, respectively. The different surface atom arrangements and degrees of surface-coordinative unsaturation of the cations and anions lead to the differences in oxygen vacancy formation energy, interaction strength with surface adsorbates, and different surface areas. Though the matter is still under debate, recently, a strong correlation between the surface area and the number and size of surface defects are suggested involving classic Weibull statistics.[23] The appreciable high surface area of Ce-3 is definitely a boosting parameter behind its superior catalytic activity.[24] The growth of preferential planes controls the formation of different shapes of nanocrystals.[25] The formation of exposed facets with higher surface energies may provide the active sites for catalytic reactions. The surface energies play an important part in the controlled synthesis of different shapes. Here, the desired shape is obtained using PVP as a surfactant. Tuning the amount of PVP in the reaction mixture, the formation of cubical CeO_2 is obtained instead of its intrinsic hexagonal shape with exposed {111} facet. The change in the amount of PVP is found to be highly influential in formation of CeO_2 nanocrystals. Initially, the NO_3^- ions from the precursor to the solution react strongly with (100) planes which results in anisotropic growth of (110) crystal planes. Here, PVP plays an important role by preferentially interacting with the (111) plane to (100). With the increase in the concentration of PVP in the reaction mixture, the preferential interaction of the PVP molecules with the ceria 001 planes slows the growth of {001} facets relative to {111} faces, leading to the formation of cube-like structures in Ce-3. It is reported that the cube-like structures of CeO_2 with exposed (100) planes contain higher oxygen defects which is a key factor behind the better catalytic activity. The percentages of exposed {100} facets of Ce-1 (27%), Ce-2 (32%), and Ce-3 (78%) are determined from their corresponding morphological characteristics. Oxygen vacancy is inversely proportional to the crystallite size of the material.[26] Surface catalytic activity also depends on the lattice strain of the material. With the increase in lattice strain, catalytic activity increases. It can enhance the performance of the catalyst by decreasing the strength of the metal−oxygen bond.[27] In Table 2, it is seen that for Ce-3, the crystallite size is

Table 2. Crystallite Size and Lattice Strain of Different Samples of Ce

sample	crystallite size (nm)	lattice strain
Ce-1	11.87	0.012
Ce-2	11.01	0.013
Ce-3	10.05	0.020

lowest, while the lattice strain is highest. It concurs with the better performance of Ce-3 than Ce-1 and Ce-2 toward MB degradation.

Spectroscopic Analysis. The prepared CeO_2 materials are then spectroscopically analyzed to investigate their catalytic performances. Figure 3a presents the UV−visible absorption characteristics of Ce-1, Ce-2, and Ce-3 where a bathochromic shift is observed for Ce-3. The shifting of absorption edge to longer wavelength often has a correlation to alternation in the band gap of the respective material.[28] The band gap energies of the CeO_2 materials of different shapes were then obtained by plotting Schuster−Kubelka−Munk absorption function, $(\alpha h\nu)1/n$ against the photon energy ($h\nu$) according to eq 2

$$(\alpha h\nu)1/n = A(h\nu - E_g) \quad (2)$$

where A is a proportionality constant, h is Planck's constant, n ($n = 2$ here for direct transition) is the frequency of vibration (hence $h\nu$ is photon energy), and α is an absorption coefficient. The band gaps are determined from the straight line x-intercept as presented in Figure 3b, showing that the band gaps are 3.17, 3.08, and 1.93 eV for Ce-1, Ce-2, and Ce-3, respectively. In general, the band gap of CeO_2 is ≥3 eV, while in cuboidal CeO_2, Ce-3, the band gap is found to be highly reduced. The greater oxygen vacancies in Ce-3 result in narrowing band gap and thus increase the light absorption of the Ce-3, which is simultaneously found to be more efficient toward MB degradation than Ce-1 and Ce-2. The characteristic major UV−visible peak of CeO_2 is seen at 363 nm in Figure 3a.

A hump-like absorption peak around 640 nm for Ce-3 corresponds to its narrow band gap too [Figure 3a]. Oxygen vacancy has also a strong influence in narrowing of band gap in CeO_2. The presence of oxygen vacancies is confirmed using PL spectroscopy in Figure 4 using excitation wavelength 320 nm. The formation of oxygen vacancies in CeO_2 is represented by Kroger−Vink equation,[29] $O_x^o + 2Ce_{Ce}^x = V_o^{\bullet\bullet} + 2Ce'_{Ce} + 1/2O_2$, where O_x^o is the O^{2-} ion on the oxygen lattice site. Ce_{Ce}^x and Ce'_{Ce} are Ce^{4+} and Ce^{3+}, respectively, and $V_o^{\bullet\bullet}$ is doubly charged oxygen vacancy and releases two free electrons. These free electrons are captured by Ce^{4+} and become Ce^{3+} ions. The resulted oxygen vacancies generating Ce^{3+} ions lead to a lattice distortion which has a direct correlation with the narrowing of band gap of the sensing material. Reportedly, the emission energy is 3.0−3.38 eV for the de-excitation of the electrons to the valence band (VB) in cerium oxides. The PL emissions are thus expected to be the transition from the 4f band of Ce to the 2p band of O, and the emission peaks ranging from 350 to 575 nm, observed in Figure 4, are assigned to the results of defects including oxygen vacancies.[30−32] The surface reactivity of CeO_2 nanostructures can also be warranted in the light of their PL

DOI: 10.1021/acsomega.8b03298
ACS Omega 2019, 4, 4243−4251

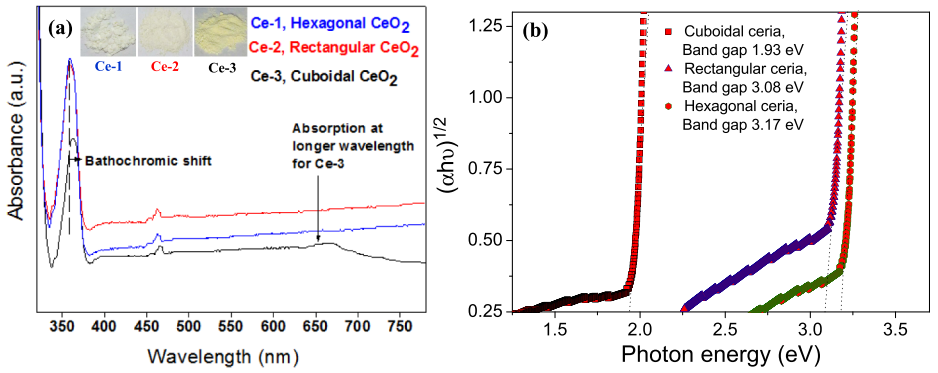

Figure 3. (a) UV−vis spectroscopy and (b) Schuster−Kubelka−Munk absorption function of CeO_2 nanostructures, showing the band gap energies of different shapes of ceria.

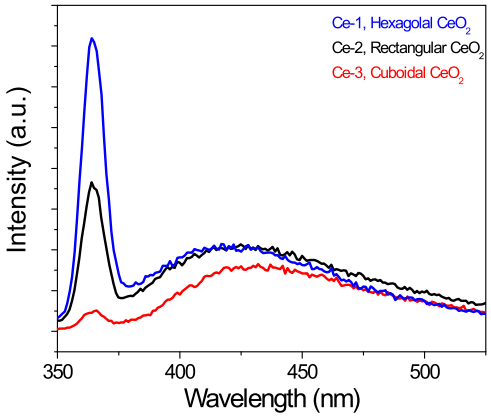

Figure 4. PL spectroscopy of different shapes of CeO_2 nanostructures.

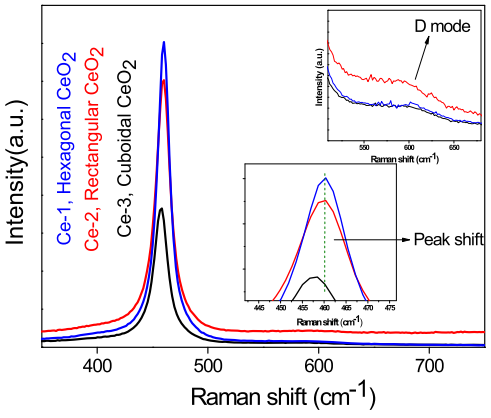

Figure 5. Raman spectroscopy of different shapes of CeO_2 nanostructures, Ce-1, Ce-2 and Ce-3.

spectroscopic analysis. In Figure 4, the emission peaks for all the samples, Ce-1, Ce-2, and Ce-3, were found to be near the same region and the order of separation efficiency of photoexcited holes and electrons was found to be Ce-3 > Ce-2 > Ce-1. The energy gap between the VB and conduction band (CB) is different for different facets. The electronic structure, especially the oxygen vacancies, determines the efficiency of photon absorption. The increase in catalytic activity of cuboidal CeO_2, that is, Ce-3, may be assigned to the charge separation efficiency between an electron and hole pair.[33] Because the PL emission spectra deal with the recombination of excited electrons and holes, a higher PL intensity indicates a higher recombination rate of electron−hole pairs under the irradiation. In Figure 4, Ce-1 and Ce-2 possessed much higher intensity indicating the fastest recombination rate of electrons and holes in the materials, while for Ce-3, the PL emission intensity is highly decreased. It supports the better catalytic efficiency of cubical ceria. As discussed previously, the high oxygen vacancies present in Ce-3 facilitate the charge carrier localization and hence prolonged separation by trapping at energy levels close to the conduction or VBs. As a consequence, the lifetime of the electron−hole separation is increased. In support of the PL study, Raman spectroscopic analyses also site justification for the better catalytic performance of Ce-3 than Ce-1 and Ce-2, presented in Figure 5 where the characteristic band around 460 cm^{-1} is observed for all the CeO_2 samples. The 460 cm^{-1} band is indexed to the Raman-active vibrational mode (F_{2g}) of the FCC structure. It arises because of a symmetrical stretching vibration of the oxygen atoms around cerium ions.[34] The higher full width at half-maxima and lower intensity of the Raman peak at 460 cm^{-1} for Ce-3 are associated with smaller crystallite size which is also consistent with the crystallite size calculation from XRD (Figure S1). The decrease in the intensity for cuboidal CeO_2 and shift toward lower frequency (inset right down Figure 5) may be corroborated as a result of asymmetry induced by randomly oriented oxygen vacancies, which in turn increases the catalytic activity. A weak band around 600 cm^{-1} (inset right up Figure 5) belongs to defect-induced (D) mode of CeO_2 nanostructures. Reportedly,[35] the ratio of the intensities of the D and F_{2g} bands, that is, I_D/I_{F2g} values, bears a directly proportional relation with oxygen vacancies. Here, the greater values of I_D/I_{F2g} of Ce-3 than those of Ce-2 and Ce-1 support again the presence of higher oxygen vacancies in cuboidal ceria nanostructures. To envisage the enhanced electron−hole separation and catalytic activity of the materials, the X-ray photoelectron spectroscopy (XPS) was performed. Figure 6a−c shows the core-level Ce 3d spectra of Ce-1, Ce-2, and Ce-3, respectively. They show the characteristic peaks of Ce^{3+} at 885.7, 899, and 904.3 eV and the other peaks at 882.2, 901.1, and 916.1 eV, could be assigned to the +4 oxidation state of CeO_2.[36] The materials are found to contain the mix valence states. In FCC-type CeO_2 nanostructures, a Ce^{4+} ion is always surrounded by eight O^{2-} ions.[37] As reported by Voskanyan et al., the existence of the oxygen vacancies and the accompanying Ce^{3+} reduces the coordination number of cerium from eight to seven which causes the change in the Ce−O bond length and overall lattice constant. Their study reveals a quantifiable approach regarding the XPS

DOI: 10.1021/acsomega.8b03298
ACS Omega 2019, 4, 4243−4251

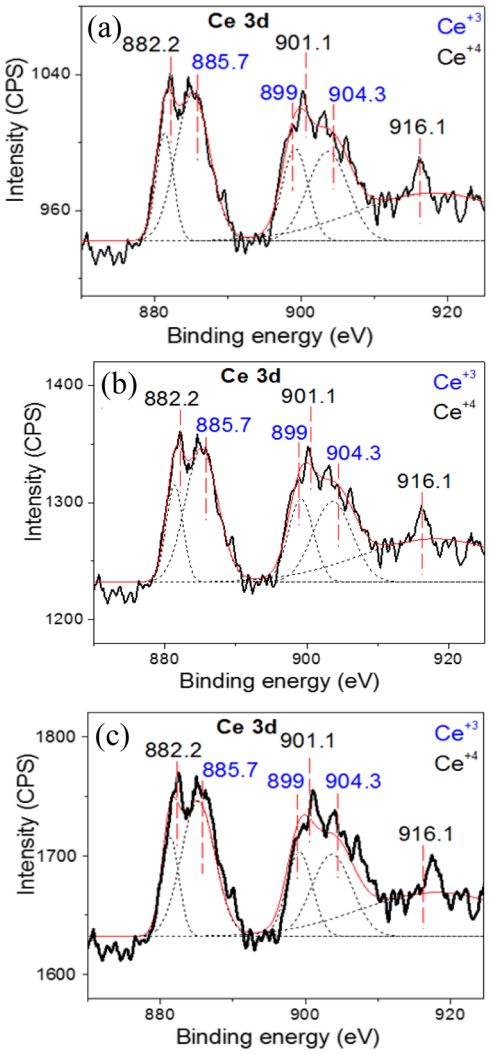

Figure 6. (a–c) Ce 3d core-level XPS peaks of Ce-1, Ce-2, and Ce-3, respectively.

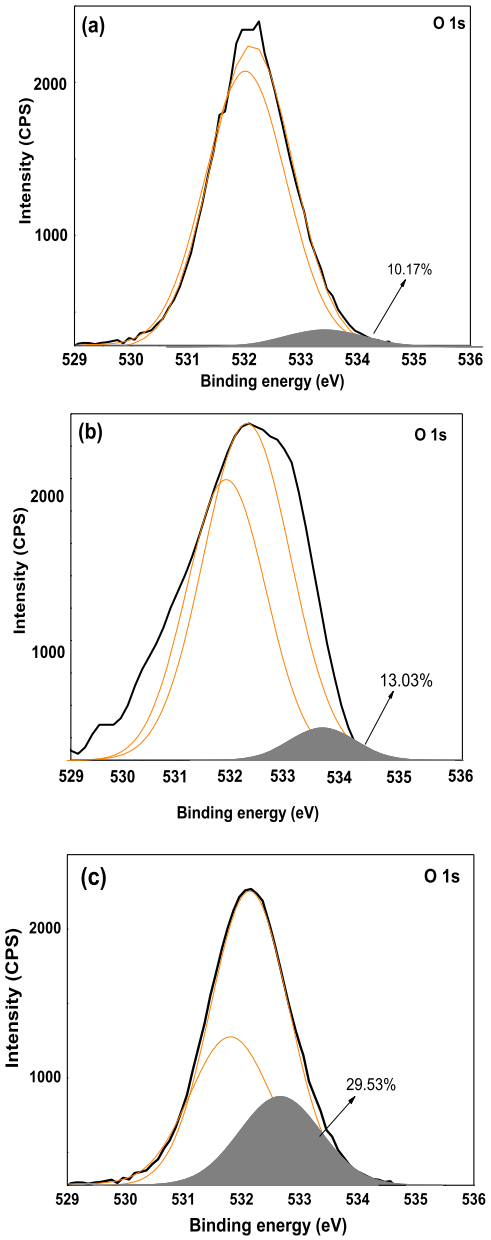

Figure 7. (a–c) O 1s core-level XPS peaks of Ce-1, Ce-2, and Ce-3, respectively.

results showing that CeO_2 containing higher percentage (34.9%) of $Ce^{3\pm}$ ions shows better catalytic activity. In our case, the cuboidal CeO_2 [Figure 6c] is calculated to have much higher percentage of Ce^{3+} (~32%) than rectangular (~16.54%) and hexagonal (~14.01%) CeO_2 nanostructures, as presented in Figure 6b,a and respectively. XPS profiles of O 1s are presented in Figure 7 where two Gaussian peaks represent a low binding energy peak at ~531 eV (lattice oxygen) and a high binding energy peak at ~533 eV (chemisorbed oxygen). Chemisorbed oxygen is directly proportional to the oxygen vacancies.[38−41] Here, in Figure 7a,b, the representative plot of chemisorbed oxygen of Ce-1 and Ce-2 are 10.17 and 13.03%, respectively, while it is greater for Ce-3 (29.53%). Therefore, besides the appreciable percentage of Ce^{3+}, a greater amount of chemisorbed oxygen species reconfirms the evolution of higher oxygen vacancies in Ce-3, making it more potential toward superior catalytic activity than Ce-1 and Ce-2.

Catalysis. As discussed in the catalytic activity test, photocatalytic degradation of MB was performed deploying Ce-1, Ce-2, and Ce-3 under irradiation with UV light, as shown in Figure 8a–c. Figure 8a,b shows the catalytic performance of Ce-1 and Ce-2 for degradation of MB at pH~3 under the UV light irradiation of wavelength ~253 nm. The peak intensity at 663 nm does not change significantly even after 200 min of UV light irradiation for both the cases. In Figure 8c, the excellent photo catalytic performance of Ce-3 is observed resulting in complete degradation of MB within 175 min. The same set of catalytic experiments was performed under dark using catalysts and without using catalysts. The corresponding results are presented in Figures 9 and 10, respectively. The enhanced catalytic performance of Ce-3 than Ce-1 and Ce-2 is explained on the basis of different electronic configurations which is the key factor behind the rapid degradation of MB. It is already mentioned and discussed that the greater oxygen vacancies in Ce-3 may have decreased the gap between VB and CB. Thus, in the presence of UV light, the electrons of Ce-3 are easily being excited to the CB from the valence band to react with the surface O_2 and H_2O of CeO_2 to generate superoxide anions ($O_2^{\bullet-}$) and hydroxyl ions ($OH^{\bullet}$)

DOI: 10.1021/acsomega.8b03298
ACS Omega 2019, 4, 4243−4251

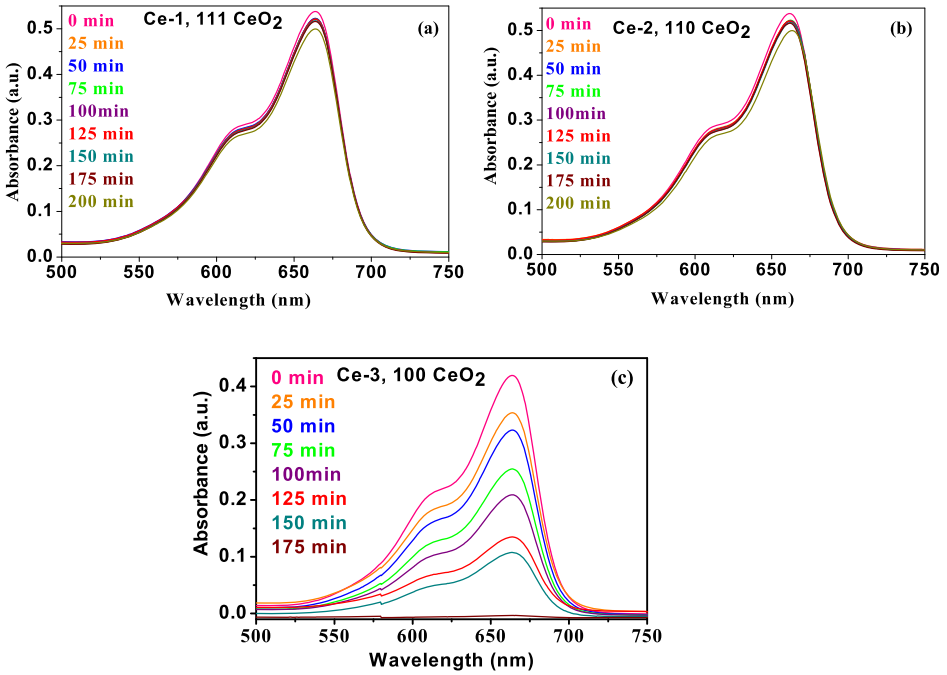

Figure 8. (a–c) MB degradation under the UV source using Ce-1, Ce-2, and Ce-3, respectively.

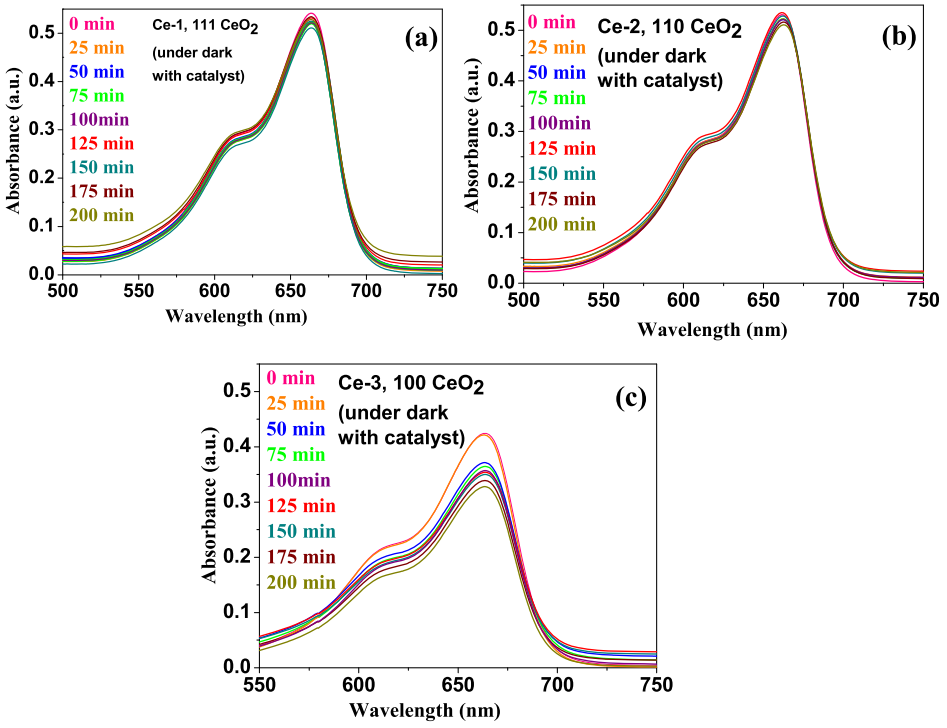

Figure 9. (a–c) MB degradation under dark using Ce-1, Ce-2, and Ce-3, respectively.

respectively which are responsible for degradation of MB. The photodegradation mechanism of MB over the different facets of CeO_2 is mainly governed by the surface reactivity of different facets. Reportedly, two pathways of photodegradation of MB may be proposed.[19] Under the photo-excitation of the VB, electrons hop to the band gap, CB, generating holes in the VB. Now, these holes upon reaction with water molecules, or hydroxide ions, will generate $OH^{\bullet}$. These radicals cause the degradation process MB.[42] Additionally, the oxygen vacancies associated with metal-oxide nanoparticles are also held responsible indirectly for the degradation. The availability of oxygen vacancies plays the key role behind the adsorption of water molecules as oxygen atom creates two bridging OH^{-} groups per initial vacancy, resulting in a transfer of proton to that water molecule. Therefore, oxygen vacancies in the CeO_2 structures can be assigned as the active sites for water dissociation. Therefore, oxygen vacancy is directly proportional to MB degradation. Again, oxygen vacancy on different facets of CeO_2 is different. According to XPS, PL, and Raman spectroscopic results, it is very much evident that cube-like Ce-

DOI: 10.1021/acsomega.8b03298
ACS Omega 2019, 4, 4243–4251

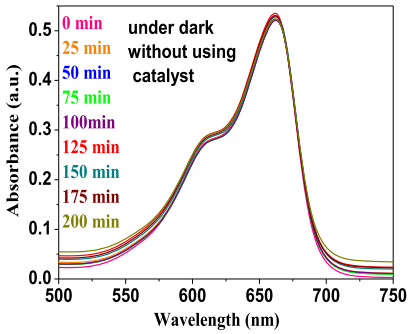

Figure 10. MB degradation under dark without using a catalyst.

3 nanomaterial bearing exposed (100) facets contain the greater oxygen vacancies than Ce-2 and Ce-1. As discussed previously, according to DFT calculations,[43,44] the required amount of energy to form oxygen vacancies on (111) is greater than that on (110) and (100).[45] Subsequently, the facet bears more oxygen vacancy and will cause better degradation of MB. Thus, being governed by the availability of oxygen vacancies, the experimentally proved efficiency of different facets of CeO_2 follows the order (100) > (110) > (111). Thus, CeO_2 having more exposed (100) will show better photodegradation of MB. Here, cube-like Ce-3 nanostructures bearing the predominantly exposed (100) facet shows better photodegradation efficiency than Ce-2 and Ce-1. In order to understand the photodegradation rate of MB in the presence and absence of CeO_2, we have plotted the relative concentration (C_t/C_0) against the UV irradiation time in Figure 11a. We have found that the complete discoloration of MB in the presence of UV light takes place exponentially with a first-order rate equation with a calculated kinetic rate constant (κ) of 1.21×10^{-2} min^{-1}. To understand the stability of Ce-3 without losing its activity, we conducted three consecutive cycles without further addition of the sample which is shown in Figure 11b. It shows that the photocatalytic efficiency of the sample remains almost the same after three consecutive cycles which indicates the high stability of the Ce-3 sample. As the catalytic efficiency remains almost constant after each cycle, it may be applied many times in the textile industry for the purification of MB contaminated water. The proposed mechanism is as follows

$$CeO_2 + h\gamma \rightarrow e_{CB}^- + h_{VB}^+$$

$$e_{CB}^- + O_2 \rightarrow O_2^{\bullet -}$$

$$O_2^{\bullet -} + MB \rightarrow \text{product}$$

$$h_{VB}^+ + H_2O \rightarrow HO^{\bullet} + H_{aq}^+$$

$$HO^{\bullet} + MB \rightarrow \text{product}$$

Besides the degradation of MB, it is very much important to envisage the corresponding degradation pathway of the same under the catalytic condition. The mass spectra before and after MB degradation is presented in Figure 11a,b, respectively. The decolorized solution, decreased peak intensity of MB, and the appearances of new peaks of different molecular weights (m/z ratios) in post-degradation mass spectra reconfirm the photodegradation of MB. Corresponding to the respective molecular weights, found in post degradation spectra Figure 11b a plausible set of compounds are identified.[19] The degraded fragmented moieties, providing a plausible degradation mechanism of MB according to their decrease in molecular weight, are included in Figure S4. For better manifestation of the developed catalyst, Ce-3, a comparative analysis is presented in Table S1, showing the MB degradation efficiency of different CeO_2 based materials (Figure 12).

CONCLUSIONS

An environmentally benign synthesis method of CeO_2 nanoparticles is reported highlighting the contribution of PVP as an additive behind the formation of the most surface-reactive {100} facet which results in cube-like CeO_2 structures of high surface area (~900 cc/g). Tailoring the crystallographic structures of CeO_2, narrowing of band gap upto 1.93 eV is achieved and the oxygen vacancies are also spectroscopically investigated which resulted in a notable change in the corresponding catalytic activity toward the MB degradation. Besides the development of an undoped CeO_2 material for MB photodegradation with appreciable efficiency, the effect of different facets of CeO_2 is thoroughly studied for the same.

EXPERIMENTAL SECTION

Materials. Ammonium cerium(IV) nitrate [$(NH_4)_2Ce(NO_3)_6$, ≥98.5%] is purchased from Sigma-Aldrich. PVP ≥99.8% and ethylene glycol (EG) (anhydrous, $HOCH_2CH_2OH$, ≥99.8%) were procured from Loba Chemie Pvt. Ltd., India. Deionized water was used throughout the synthesis and washing. For photocatalysis, MB is purchased from Sigma-Aldrich. All the reagents are of analytical grade.

Methods. In a typical procedure, CeO_2 was synthesized via the precipitation method taking ammonium cerium(IV) nitrate as the precursor material. Solution of $(NH_4)_2Ce(NO_3)_6$ (0.009 mol %) was prepared in 30 mL EG, and it was kept under a

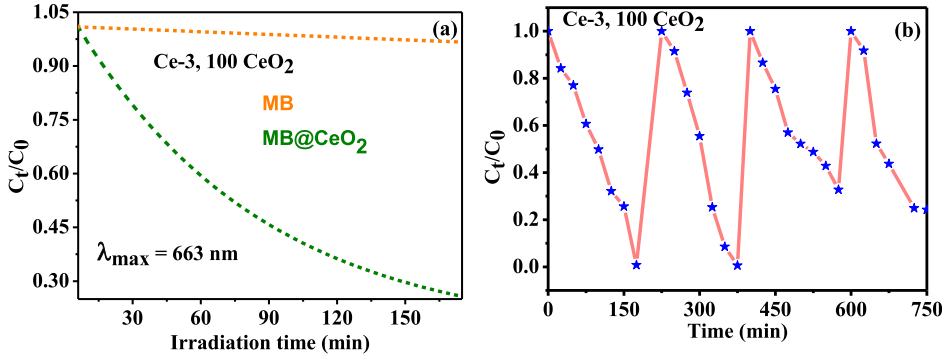

Figure 11. (a) Rate of degradation of MB in UV light in the presence of Ce-3 and (b) recyclability test of the same using Ce-3 as a catalyst.

DOI: 10.1021/acsomega.8b03298
ACS Omega 2019, 4, 4243−4251

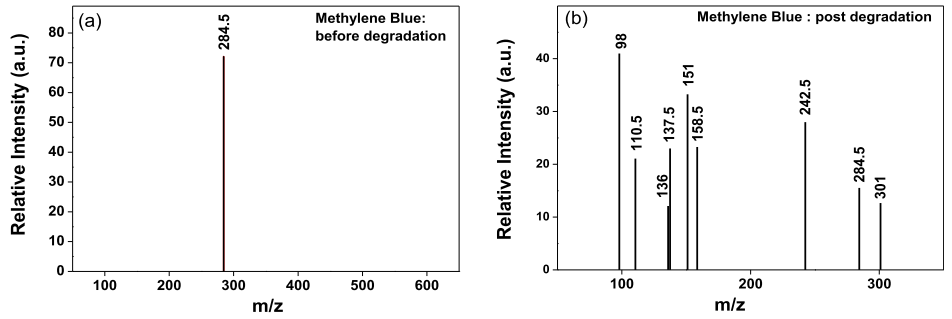

Figure 12. (a) Mass spectroscopic results before (a) and after (b) degradation of MB.

vigorous stirring condition till the solution became clear. Then, 0.25, 0.5, and 1.26 g PVP were added to the solution differently and marked as Ce-1, Ce-2, and Ce-3, respectively. After the addition of PVP, the solution was refluxed at 190 °C for 4 h under a vigorous stirring condition. For each case to collect the sample, the mixture was centrifuged and washed with deionized water. Finally, the collected samples were dried overnight under vacuum.

Characterization Techniques. The structural morphology of the synthesized materials was investigated using high-resolution TEM (model: TECNAI G2 30ST; manufacturer: FEI Company, The Netherlands). Crystallographic characteristics of the materials were examined using an X-ray diffractometer with the Cu Kα line (model: D8 ADVANCE; manufacturer: Bruker Corporation, MA, USA) and XPS (model: PHI 5000 Versa probe II XPS system) having a source of Al Kα and charge neutralizer at room temperature. The nitrogen adsorption−desorption isotherms of the materials are measured using Quantachrome Instruments version3.0. The base pressure was maintained at 6×10^{-10} mbar with an energy resolution of 0.6 eV. The Raman spectroscopic analysis was performed using Renishaw Raman System 1000 calibrated using a silicon standard. Mass spectroscopic results were obtained using liquid chromatography−mass spectrometry (Waters 2695, USA) spectrometer.

Catalytic Activity Test. With the decrease in absorbance of the target analyte, MB was monitored using UV−vis spectroscopy where the peak at 663 nm was the characteristic peak of MB. The comparative photocatalytic degradation of MB using Ce-1, Ce-2, and Ce-3 had been carried out using an 8 W UV lamp of wavelength 253 nm. Three different samples were mixed with MB in a 1:1 ratio (4.6 μM each) separately in a continuously stirring condition for 30 min in a quartz cuvette, maintaining pH ≈ 3. Then, the cuvette was placed at ∼2 cm apart from the UV light source and the UV light was turned on. The absorbance of MB was measured at a certain interval of time in a UV−vis spectrophotometer and the absorbance at 663 nm was monitored for each sample to measure the comparative photocatalytic degradation efficiency. Getting the complete degradation of MB using the Ce-3 sample, we added the same amount of MB (4.6 μM) to the solution mixture after completing every cycle without further addition of our sample for recyclability test.

■ ASSOCIATED CONTENT

Supporting Information

The Supporting Information is available free of charge on the ACS Publications website at DOI: 10.1021/acsomega.8b03298.

XRD measurements of three differently faceted CeO_2 nanostructures for crystallographic analysis, TEM micrographs showing the formation of hexagonal, rectangular, and cuboidal shape of CeO_2 nanoparticles, BET surface area measurements for representation of effective surface area and pore size distribution, and tentative pathways of MB degradation (PDF)

■ AUTHOR INFORMATION

Corresponding Author

*E-mail: sroy@cgcri.res.in. Phone: +91 33 23223427.

ORCID

Somenath Roy: 0000-0002-3352-0534

Notes

The authors declare no competing financial interest.

■ ACKNOWLEDGMENTS

The research presented in the article was partially funded by the Council of Scientific and Industrial Research (CSIR), Government of India, through the 12th five year plan network project "MULTIFUN" (grant number: CSC-0101) and DST Nanomission, Government of India [grant number: SR/NM/NT-1001/2015(C)]. The author D.M. gratefully acknowledges her INSPIRE fellowship of Department of Science and Technology (DST), Government of India, and the facilities of DST-CSIR Sensor Hub, CGCRI, Kolkata, and S. N. Bose National Centre for Basic Sciences, Kolkata.

■ REFERENCES

(1) Rauf, M. A.; Ashraf, S. S. Fundamental principles and application of heterogeneous photocatalytic degradation of dyes in solution. *Chem. Eng. J.* **2009**, *151*, 10−18.

(2) Houas, A.; Lachheb, H.; Ksibi, M.; Elaloui, E.; Guillard, C.; Herrmann, J. M. Photocatalytic degradation pathway of methylene blue in water. *Appl. Catal., B* **2001**, *31*, 145−157.

(3) Kim, S. D.; Cho, J.; Kim, I. S.; Vanderford, B. J.; Snyder, S. A. Occurrence and removal of pharmaceuticals and endocrine disruptors in South Korean surface, drinking, and waste waters. *Water Res.* **2007**, *41*, 1013−1021.

(4) Liu, Q. Y.; Liu, Y. X.; Lu, X. J. Combined Photo-Fenton and Biological Oxidation for the Treatment of Aniline Wastewater. *Procedia Environ. Sci.* **2012**, *12*, 341.

(5) Oller, I.; Malato, S.; Sánchez-Pérez, J. A. Combination of Advanced Oxidation Processes and biological treatments for wastewater decontamination-A review. *Sci. Total Environ.* **2011**, *409*, 4141−4166.

(6) W. H., Wells; V. L., Wells *Patty's Toxicology*; John Wiley & Sons, Inc., 2001.

(7) Pandit, V. U.; Arbuj, S. S.; Pandit, Y. B.; Naik, S. D.; Rane, S. B.; Mulik, U. P.; Gosavi, S. W.; Kale, B. B. Solar light driven dye

DOI: 10.1021/acsomega.8b03298
ACS Omega 2019, 4, 4243−4251

degradation using novel organo-inorganic (6,13-pentacenequinone/TiO2) nanocomposite. *RSC Adv.* **2015**, *5*, 10326−10331.
(8) Sayle, D. C.; Maicaneanu, S. A.; Watson, G. W. Atomistic Models for CeO2(111), (110), and (100) Nanoparticles, Supported on Yttrium-Stabilized Zirconia. *J. Am. Chem. Soc.* **2002**, *124*, 11429−11439.
(9) Jiang, Y.; Adams, J. B.; van Schilfgaarde, M. Density-functional calculation of CeO2 surfaces and prediction of effects of oxygen partial pressure and temperature on stabilities. *J. Chem. Phys.* **2005**, *123*, 064701.
(10) Chen, Y.; Hu, P.; Lee, M.-H.; Wang, H. Au on (111) and (110) surfaces of CeO2: A density-functional theory study. *Surf. Sci.* **2008**, *602*, 1736−1741.
(11) Sayle, T. X. T.; Cantoni, M.; Bhatta, U. M.; Parker, S. C.; Hall, S. R.; Möbus, G.; Molinari, M.; Reid, D.; Seal, S.; Sayle, D. C. Strain and Architecture-Tuned Reactivity in Ceria Nanostructures; Enhanced Catalytic Oxidation of CO to CO2. *Chem. Mater.* **2012**, *24*, 1811−1821.
(12) Abid, M.; Paul-Boncour, V.; Touroude, R. Pt/CeO2 catalysts in crotonaldehyde hydrogenation: Selectivity, metal particle size and SMSI states. *Appl. Catal., A* **2006**, *297*, 48−59.
(13) Zhou, X.-D.; Huebner, W.; Anderson, H. U. Processing of Nanometer-Scale CeO2 Particles. *Chem. Mater.* **2003**, *15*, 378−382.
(14) Mai, H.-X.; Sun, L.-D.; Zhang, Y.-W.; Si, R.; Feng, W.; Zhang, H.-P.; Liu, H.-C.; Yan, C.-H. Shape-selective synthesis and oxygen storage behavior of ceria nanopolyhedra, nanorods, and nanocubes. *J. Phys. Chem. B* **2005**, *109*, 24380−24385.
(15) Zhou, K.; Yang, Z.; Yang, S. Highly Reducible CeO2Nanotubes. *Chem. Mater.* **2007**, *19*, 1215−1217.
(16) Pouretedal, H. R.; Kadkhodaie, A. Synthetic CeO2 Nanoparticle Catalysis of Methylene Blue Photodegradation: Kinetics and Mechanism. *Chin. J. Catal.* **2010**, *31*, 1328−1334.
(17) Liu, C. B.; Qian, J. C.; Chen, F.; Wu, Z. Y.; Chen, Z. G. Facile Synthesis of Highly Ordered Macroporous CeO2 Film for Methylene Blue Degradation. *Mater. Sci. Forum* **2014**, *787*, 41−45.
(18) Channei, D.; Inceesungvorn, B.; Wetchakun, N.; Ukritnukun, S.; Nattestad, A.; Chen, J.; Phanichphant, S. Photocatalytic degradation of methyl orange by CeO2 and Fe-doped CeO2 films under visible light irradiation. *Sci. Rep.* **2014**, *4*, 5757.
(19) Rouby, W. M. A. E.; Farghali, A. A.; Hamdedein, A. Microwave synthesis of pure and doped cerium (IV) oxide (CeO2) nanoparticles for methylene blue degradation. *Water Sci. Technol.* **2016**, *74*, 2325−2336.
(20) Omata, T.; Ono, K.; Otsuka-Yao-Matsuo, S. Photodegradation of Methylene Blue Aqueous Solution Sensitized by Pyrochlore-Related κ-CeZrO. *Mater. Trans.* **2003**, *44*, 1620−1623.
(21) Saikia, P.; Miah, A. T.; Das, P. P. Highly efficient catalytic reductive degradation of various organic dyes by Au/CeO2-TiO2 nano-hybrid. *J. Chem. Sci.* **2017**, *129*, 81−93.
(22) Tumuluri, U.; Rother, G.; Wu, Z. Fundamental Understanding of the Interaction of Acid Gases with CeO_2: From Surface Science to Practical Catalysis†. *Ind. Eng. Chem. Res.* **2016**, *55*, 3909.
(23) Roy, A.; Mead, J.; Wang, S.; Huang, H. Effects of surface defects on the mechanical properties of ZnO nanowires. *Sci. Rep.* **2017**, *7*, 9547.
(24) Wang, H.; Yang, L.; Yu, H.; Peng, F. A Highly Efficient and Stable Visible-Light Plasmonic Photocatalyst Ag-AgCl/CeO2. *World J. Nano Sci. Eng.* **2011**, *1*, 129−136.
(25) Zhang, J.; Ohara, S.; Umetsu, M.; Naka, T.; Hatakeyama, Y.; Adschiri, T. Colloidal Ceria Nanocrystals: A Tailor-Made Crystal Morphology in Supercritical Water. *Adv. Mater.* **2007**, *19*, 203−206.
(26) Jha, A.; Jeong, D. W.; Lee, Y. L.; Nah, I. W.; Roh, H. S. Enhancing the catalytic performance of cobalt oxide by doping on ceria in the high temperature water-gas shift reaction. *RSC Adv.* **2015**, *5*, 103023−103029.
(27) Zhao, F.; Liu, Z.; Xu, W.; Yao, S.; Kubacka, A.; Johnston- Peck, A. C.; Senanayake, S. D.; Zhang, A.-Q.; Stach, E. A.; García, M. F.; Rodriguez, J. A. Water-Gas Shift Reaction on Ni−W−Ce Catalysts: Catalytic Activity and Structural Characterization. *J. Phys. Chem. C* **2014**, *118*, 2528.
(28) Wang, J.; Wang, Z.; Huang, B.; Ma, Y.; Liu, Y.; Qin, X.; Zhang, X.; Dai, Y. Oxygen Vacancy Induced Band-Gap Narrowing and Enhanced Visible Light Photocatalytic Activity of ZnO. *ACS Appl. Mater. Interfaces* **2012**, *4*, 4024−4030.
(29) Shoko, E.; Smith, M. F.; McKenzie, R. H. Charge distribution near bulk oxygen vacancies in cerium oxides. *J. Phys.: Condens. Matter* **2010**, *22*, 223201.
(30) Corma, A.; Atienza, P.; Garcia, H.; Chane-Ching, J. Y. Hierarchically mesostructured doped CeO2 with potential for solar cell use. *Nat. Mater.* **2004**, *3*, 394−397.
(31) Yu, S.-H.; Colfen, H.; Fischer, A. High quality CeO2 nanocrystals stabilized by a double hydrophilic block copolymer. *Colloids Surf., A* **2004**, *243*, 49−52.
(32) Morshed, A. H.; Moussa, M. E.; Bedair, S. M.; Leonard, R.; Liu, S. X.; Masry, N. E. Violet/blue emission from epitaxial cerium oxide films on silicon substrates. *Appl. Phys. Lett.* **1997**, *70*, 1647.
(33) Taniguchi, T.; Sonod, Y.; Echikawa, M.; Watanabe, Y.; Hatakeyama, K.; Ida, S.; Koinuma, M.; Matsumoto, Y. Intense Photoluminescence from Ceria-Based Nanoscale Lamellar Hybrid. *ACS Appl. Mater. Interfaces* **2012**, *4*, 1010−1015.
(34) Mukherjee, D.; Venkataswamy, P.; Devaiah, D.; Rangaswamy, A.; Reddy, B. M. Crucial role of titanium dioxide support in soot oxidation catalysis of manganese doped ceria. *Catal. Sci. Technol.* **2017**, *7*, 3045.
(35) Han, J.; Meeprasert, J.; Maitarad, P.; Nammuangruk, S.; Shi, L.; Zhang, D. Investigation of the Facet-Dependent Catalytic Performance of Fe_2O_3/CeO_2 for the Selective Catalytic Reduction of NO with NH_3. *J. Phys. Chem. C* **2016**, *120*, 1523−1533.
(36) Majumder, D.; Datta, A.; Mitra, M. K.; Roy, S. Kinetic analysis of low concentration CO detection by Au-loaded cerium oxide sensors. *RSC Adv.* **2016**, *6*, 92989−92995.
(37) Voskanyan, A. A.; Chan, K.-Y.; Vanessa Li, C.-Y. Colloidal Solution Combustion Synthesis: Toward Mass Production of a Crystalline Uniform Mesoporous CeO2 Catalyst with Tunable Porosity. *Chem. Mater.* **2016**, *28*, 2768−2775.
(38) Zhao, X.; Lu, M.; Li, H.; Fang, J.; Shi, L.; Zhang, D. In situ preparation of Ni nanoparticles in cerium-modified silica aerogels for coking- and sintering-resistant dry reforming of methane. *New J. Chem.* **2017**, *41*, 4869−4878.
(39) Wang, N.; Shen, K.; Huang, L.; Yu, X.; Qian, W.; Chu, W. Facile Route for Synthesizing Ordered Mesoporous Ni−Ce−Al Oxide Materials and Their Catalytic Performance for Methane Dry Reforming to Hydrogen and Syngas. *ACS Catal.* **2013**, *3*, 1638−1651.
(40) Zang, C.; Zhang, X.; Hu, S.; Chen, F. The Role of Exposed Facets in the Fenton-like Reactivity of CeO2 Nanocrystal to the Orange II. *Appl. Catal., B* **2017**, *216*, 106−113.
(41) Du, X.; Zhang, D.; Shi, L.; Gao, R.; Zhang, J. Morphology Dependence of Catalytic Properties of Ni/CeO_2 Nanostructures for Carbon Dioxide Reforming of Methane. *J. Phys. Chem. C* **2012**, *116*, 10009−10016.
(42) Rauf, M. A.; Ashraf, S. S. Fundamental principles and application of heterogeneous photocatalytic degradation of dyes in solution. *Chem. Eng. J.* **2009**, *151*, 10−18.
(43) Abid, M.; Paul-Boncour, V.; Touroude, R. Pt/CeO2 catalysts in crotonaldehyde hydrogenation: Selectivity, metal particle size and SMSI states. *Appl. Catal., A* **2006**, *297*, 48−59.
(44) Zhang, D.; Du, X.; Shia, L.; Gaoa, R. Shape-controlled synthesis and catalytic application of ceria nanomaterials. *Dalton Trans.* **2012**, *41*, 14455−14475.
(45) Apostolescu, N.; Apostolescu, G. A.; Cernatescu, C.; Cobzaru, C.; Tataru-Farmus, R. E. Studies on the photocatalytic degradation of organic dyes using CeO_2-ZnO mixed oxides. *Environ. Eng. Manage. J.* **2015**, *14*, 415−420.

DOI: 10.1021/acsomega.8b03298
ACS Omega 2019, 4, 4243−4251